IOP Publishing Journal of Physics A: Mathematical and Theoretical

J. Phys. A: Math. Theor. **53** (2020) 125201 (21pp) https://doi.org/10.1088/1751-8121/ab749b

Application of the saddle-point method to strong-laser-field ionization

A Jašarević[1], E Hasović[1], R Kopold[2], W Becker[3,4] and D B Milošević[1,5,3]

[1] Faculty of Science, University of Sarajevo, Zmaja od Bosne 35, 71000 Sarajevo, Bosnia and Herzegovina
[2] Maxstr. 20, 93093 Donaustauf, Germany
[3] Max-Born-Institut, Max-Born-Str. 2a, 12489 Berlin, Germany
[4] National Research Nuclear University (MEPhI), Kashirskoe Shosse 31, 115409, Moscow, Russia
[5] Academy of Sciences and Arts of Bosnia and Herzegovina, Bistrik 7, 71000 Sarajevo, Bosnia and Herzegovina

E-mail: milo@bih.net.ba

Received 3 December 2019, revised 30 January 2020
Accepted for publication 10 February 2020
Published 3 March 2020

Abstract

The quantum-mechanical transition amplitude of an ionization process induced by a strong laser field is typically expressed in the form of an integral over the ionization time of a highly oscillatory function. Within the saddle-point (SP) approximation this integral can be represented by a sum over the contributions of the solutions of the SP equation for complex ionization time. It is shown that, for the general case of an elliptically polarized polychromatic laser field, these solutions can be obtained as zeros of a trigonometric polynomial of the order n and that there are exactly n relevant solutions, which are to be included in the sum. The results obtained are illustrated by examples of various tailored laser fields that are presently used in strong-field physics and attoscience. For some critical values of the parameters two SP solutions can coalesce and the topology of the 'steepest descent' integration contour changes so that some SPs are bypassed. Around the critical parameters a uniform approximation should be used instead of the SP method.

Keywords: saddle-point method, strong-field ionization, strong-field approximation, above-threshold ionization, bicircular laser field, orthogonally polarized two-color laser field, elliptically polarized laser field

(Some figures may appear in colour only in the online journal)

1. Introduction

The discovery of the chirped-pulse amplification method in the 1980s to generate high-intensity, ultra-short optical pulses has triggered the exploration of atomic processes induced by strong laser fields. Since the intensity of such laser fields is comparable with the intensity of the electric field experienced by an electron bound in an atom, the laser-induced atomic processes are highly nonlinear and cannot be treated using perturbative quantum-mechanical approaches. For the analysis of such strong-field processes, the so-called strong-field approximation (SFA) has turned out to be most useful. For the process of ionization the SFA was introduced in [1–3] and it is sometimes referred to as Keldysh–Faisal–Reiss theory; for reviews, see, e.g. [4–10].

The SFA builds on the Gordon–Volkov states [11, 12], which are exact solutions of the time-dependent Schrödinger equation for an otherwise free electron in the presence of a time-dependent laser field. Gordon–Volkov states are known in analytical form. They describe the final continuum state of an electron liberated from its initial bound state by the intense laser field and determine the quantum-mechanical ionization amplitude. In the case of strong-field ionization one has to integrate over all possible ionization times $t \in [0, T_\mathrm{p}]$, where T_p is the pulse duration. The ionization amplitude has the form $\int_0^{T_\mathrm{p}} \mathrm{d}t f(t)\mathrm{e}^{\mathrm{i}S(t)}$, with $f(t)$ and $S(t)$ real functions. The subintegral function contains the highly oscillatory factor $\mathrm{e}^{\mathrm{i}S(t)}$ where $S(t)$ is the action, which is large for high laser-field intensities and low frequencies. Straightforward evaluation of this integral, especially for long pulse duration T_p and/or low laser frequency, is impeded by these rapid oscillations. In the theory of asymptotic analysis of integrals [13, 14] such integrals are usually solved using the saddle-point or steepest-descent method. The stationarity condition $\mathrm{d}S(t)/\mathrm{d}t = 0$ leads to a nonlinear equation for the complex time t. In most cases it should be taken into account that the laser field is a periodic function of time with a period $T = 2\pi/\omega$ (ω is the fundamental frequency; in this case the integral over t is from zero to T). For a laser pulse of duration $T_\mathrm{p} = n_\mathrm{p}T$, n_p integer, the fundamental frequency is $\omega_\mathrm{p} = \omega/n_\mathrm{p}$ (see section 5.2).

Almost always, the solutions of the stationarity equation lie in the complex plane, off the original integration axis, which is the real axis. Hence, one tries to deform the original integration contour between its real endpoints 0 and T into the complex plane so that it passes through the SPs in the hope that the integral along the deformed contour is dominated by the contribution of the immediate vicinity of the complex SPs. This deformation does not change the value of the integral because of the analyticity of the functions $f(t)$ and $S(t)$. The determination of the integration path is a difficult problem [15]. Fortunately, as we will show and illustrate with examples, in most cases it is sufficient to sum over the saddle-point solutions in the upper half complex time plane taking for granted that a contour with the desired properties exists.

Recently, tailored laser fields have been used to control the microscopic electron dynamics with unprecedented spatial and temporal resolution [16]. Examples of such fields are bicircular fields, few-cycle laser fields with specified carrier-envelope phase and orthogonally polarized two-color (OTC) fields. In the case of strong-field ionization within the SFA, it is necessary to find the number of solutions of the saddle-point equation for such complex field configurations. We will show that, in addition to a simplified calculation of the highly oscillatory integrals, these solutions allow for penetrating insight into the physics of the time-dependent ionization process, enabling its control and optimization.

In this paper, we first present the transition amplitude for the strong-field ionization obtained using the SFA and then apply the saddle-point (SP) approximation to the integral

over the ionization time. Using the example of an elliptically polarized monochromatic laser field we illustrate (i) the case when the topology of the integration contour changes as a function of some parameter. At some critical value, two SP solutions temporarily merge and only one of them must be taken into account for parameter values larger than this critical value. (ii) Near this critical value, a uniform approximation has to be used, which treats both SPs on an equal footing. We discuss in detail how the contour of integration has to be deformed so as to pick up the contributions of the SPs. The number of SP solutions for the general case of the SP equation in the form of a trigonometric polynomial is analysed in the next section. The examples of the bicircular field, few-cycle laser pulse and OTC field are investigated in section 3. They illustrate how the SP analysis allows one to understand the detailed features of the electron spectra by tracing their properties to the times of ionization, which are defined on the time scale of a small fraction of the laser period. Finally, our conclusions are given in section 4. In the appendices we present the explicit forms of the matrix elements used in the numerical examples. We do not, in this paper, consider recollision processes. The atomic system of units is used throughout.

2. Theory

The quantum-mechanical transition amplitude for strong-field ionization (or detachment), within the strong-field approximation, dipole approximation and in length gauge, is determined by the integral [4, 7]

$$M_{\mathbf{p}\ell m} = -\mathrm{i}\int_{-\infty}^{\infty} \mathrm{d}t \langle \mathbf{p} + \mathbf{A}(t)|\mathbf{r}\cdot\mathbf{E}(t)|\psi_{\ell m}\rangle \mathrm{e}^{\mathrm{i}S(\mathbf{p};t)}, \tag{1}$$

where the ket vector $|\mathbf{p}\rangle$ denotes a plane wave such that $\langle \mathbf{r}|\mathbf{p}\rangle = (2\pi)^{-3/2}\mathrm{e}^{\mathrm{i}\mathbf{p}\cdot\mathbf{r}}$ and

$$S(\mathbf{p};t) = S_{\mathbf{p}}(t) + I_{\mathrm{p}}t, \quad \mathrm{d}S_{\mathbf{p}}(t)/\mathrm{d}t = \left[\mathbf{p} + \mathbf{A}(t)\right]^2/2. \tag{2}$$

The electric-field vector is $\mathbf{E}(t) = -\mathrm{d}\mathbf{A}(t)/\mathrm{d}t$. The final electron momentum and kinetic energy are $\mathbf{p}$ and $E_{\mathbf{p}} = \mathbf{p}^2/2$, respectively. The ground-state wave function is $\psi_{\ell m}$, with orbital quantum number ℓ, magnetic quantum number m and the atomic ionization potential $I_{\mathrm{p}} > 0$ (for electron detachment off a negative ion, $I_{\mathrm{p}} > 0$ is the electron affinity).

For a strong laser field the modified action $S(\mathbf{p};t)$ is large and one can apply the method of steepest descent (saddle-point (SP) method) to solve the integral over time t in (1). The SP times are determined by the condition $\partial S(\mathbf{p};t)/\partial t|_{t=t_s} \equiv S'(\mathbf{p};t_s) = 0$ and the transition amplitude is approximated by the following sum over the contributions of the SP times t_s

$$M_{\mathbf{p}\ell m} = -\mathrm{i}\sum_{t_s}\sqrt{\frac{2\pi\mathrm{i}}{S''(\mathbf{p};t_s)}}\langle \mathbf{p} + \mathbf{A}(t_s)|\mathbf{r}\cdot\mathbf{E}(t_s)|\psi_{\ell m}\rangle \mathrm{e}^{\mathrm{i}S(\mathbf{p};t_s)}, \tag{3}$$

with $S''(\mathbf{p};t_s) = \partial^2 S(\mathbf{p};t)/\partial t^2|_{t=t_s} = -\mathbf{E}(t_s)\cdot[\mathbf{p} + \mathbf{A}(t_s)]$ [17]. More details and a justification of the SP method along with its limitations will be presented below in section 3.

For a laser field with the fundamental frequency ω and the period $T = 2\pi/\omega$ we calculate the ionization rate with absorption of n photons [18–20]

$$w_{\mathbf{p}\ell}(n) = 2\pi p\sum_{m=-\ell}^{\ell}\left|T_{\mathbf{p}\ell m}(n)\right|^2, \tag{4}$$

where the T-matrix element is

$$T_{\mathbf{p}\ell m}(n) = \int_0^T \frac{\mathrm{d}t}{T} \langle \mathbf{p} + \mathbf{A}(t)|\mathbf{r}\cdot\mathbf{E}(t)|\psi_{\ell m}\rangle \mathrm{e}^{\mathrm{i}S(\mathbf{p};t)}. \tag{5}$$

In the SP approximation we have

$$T_{\mathbf{p}\ell m}(n) = \frac{1}{T}\sum_{t_s} \sqrt{\frac{2\pi\mathrm{i}}{S''(\mathbf{p};t_s)}} \langle \mathbf{p} + \mathbf{A}(t_s)|\mathbf{r}\cdot\mathbf{E}(t_s)|\psi_{\ell m}\rangle \mathrm{e}^{\mathrm{i}S(\mathbf{p};t_s)}. \tag{6}$$

The energy-conserving condition is $E_{\mathbf{p}} = n\omega - U_\mathrm{p} - I_\mathrm{p}$, where $U_\mathrm{p} = (2T)^{-1}\int_0^T \mathrm{d}t\mathbf{A}^2(t)$ is the ponderomotive energy. The modified action takes the form $S(\mathbf{p};t) = n\omega t + \mathbf{p}\cdot\boldsymbol{\alpha}(t) + U_1(t)$ with the T-periodic functions $\boldsymbol{\alpha}(t) = \int^t \mathrm{d}t'\mathbf{A}(t')$, $U_1(t) = \frac{1}{2}\int^t \mathrm{d}t'\mathbf{A}^2(t') - U_\mathrm{p}t$. Using partial integration and the fact that the Gordon–Volkov states [11, 12] $|\psi_{\mathbf{p}}(t)\rangle = |\mathbf{p} + \mathbf{A}(t)\rangle \mathrm{e}^{-\mathrm{i}S_{\mathbf{p}}(t)}$ satisfy the time-dependent Schrödinger equation $\mathrm{i}\partial|\psi_{\mathbf{p}}(t)\rangle/\partial t = \left[(-\mathrm{i}\boldsymbol{\nabla})^2/2 + \mathbf{r}\cdot\mathbf{E}(t)\right]|\psi_{\mathbf{p}}(t)\rangle$ [4], equation (5) can be written as [18, 19]

$$T_{\mathbf{p}\ell m}(n) = -\int_0^T \frac{\mathrm{d}t}{2T} \mathrm{e}^{\mathrm{i}S(\mathbf{p};t)}(\mathbf{q}^2 + \kappa^2)\tilde{\psi}_{\ell m}(\mathbf{q}) \tag{7}$$

with $\mathbf{q} = \mathbf{p} + \mathbf{A}(t)$, $\tilde{\psi}_{\ell m}(\mathbf{q}) = (2\pi)^{-3/2}\int \mathrm{d}\mathbf{r}\psi_{\ell m}(\mathbf{r})\mathrm{e}^{-\mathrm{i}\mathbf{q}\cdot\mathbf{r}}$, $S'(\mathbf{p};t) = (\mathbf{q}^2 + \kappa^2)/2$ and $I_\mathrm{p} = \kappa^2/2$. The integral over the ionization time t is calculated using standard Gauss–Legendre quadrature with a few hundred points, depending on the used laser wavelength and intensity. We will call this result 'exact'. The results obtained using the SFA and the SP approximation are valid for a wide range of laser-field parameters, mainly in the tunnelling regime but not limited to it [4–10].

3. Elliptically polarized monochromatic laser field

We will first consider an elliptically polarized laser field, since it allows us to illustrate some peculiarities of the SPs that were encountered some twenty years ago in the investigation of above-threshold ionization (ATI) [21–23]. Namely, the ellipticity distributions of liberated electrons with fixed kinetic energy were experimentally found to exhibit oscillations, which were explained to occur via the interference of the two SP contributions to the ionization probability amplitude. In the context of the present paper, the following observation is of special interest: for a fixed value of the ellipticity, there is a critical value of the electron energy after which only one SP time must be taken into account. That is, in this case the integration contour in the complex plane has to be routed only through the solution that is closest to the real axis, bypassing the other one. In this regime, the afore-mentioned oscillations go away.

The electric-field vector and the vector potential of an elliptically polarized monochromatic laser field with ellipticity ξ are

$$\mathbf{E}(t) = \frac{E_0}{\sqrt{1+\xi^2}}\left[\sin(\omega t)\hat{\mathbf{e}}_x - \xi\cos(\omega t)\hat{\mathbf{e}}_y\right], \mathbf{A}(t) = \frac{A_0}{\sqrt{1+\xi^2}}\left[\cos(\omega t)\hat{\mathbf{e}}_x + \xi\sin(\omega t)\hat{\mathbf{e}}_y\right]. \tag{8}$$

The ponderomotive energy is $U_\mathrm{p} = A_0^2/4$, with $A_0 = E_0/\omega$. For simplicity, here we only consider electrons emitted in the direction of the large component of the field, so that $\mathbf{p}\cdot\hat{\mathbf{e}}_x = p\cos\theta = p$, $\theta = 0°$. Introducing the notation $\zeta = (1-\xi^2)/(1+\xi^2)$, $\epsilon^2 = E_\mathbf{p}/(2U_\mathrm{p})$ and $\gamma^2 = I_\mathrm{p}/(2U_\mathrm{p})$ (γ is the Keldysh parameter [1]), the SP equation $S'(\mathbf{p};t_s) = 0$, i.e. $[\mathbf{p} + \mathbf{A}(t)]^2/2 + I_\mathrm{p} = 0$, can be rewritten as

$$\zeta\cos^2(\omega t)+\frac{2\epsilon}{\sqrt{1+\xi^2}}\cos(\omega t)+\epsilon^2+\frac{\xi^2}{1+\xi^2}+\gamma^2=0, \tag{9}$$

which is a quadratic equation with the two solutions

$$\cos(\omega t)=\frac{-\epsilon\pm\mathrm{i}\sqrt{D}}{\zeta\sqrt{1+\xi^2}},\quad D=\zeta\left[\gamma^2(1+\xi^2)+\xi^2\right]-\epsilon^2\xi^2. \tag{10}$$

We denote the real (imaginary) part of the complex time $t=t_\mathrm{R}+\mathrm{i}t_\mathrm{I}$ by t_R (t_I). Since equation (9) has real coefficients, with any solution ωt its complex conjugate is a solution as well.

For linear polarization, we have $D=\gamma^2>0$. We use the relation $\cos(\omega t_\mathrm{R}+\mathrm{i}\omega t_\mathrm{I})=\cos(\omega t_\mathrm{R})\cosh(\omega t_\mathrm{I})-\mathrm{i}\sin(\omega t_\mathrm{R})\sinh(\omega t_\mathrm{I})$ and find two solutions in the upper half plane having the same imaginary parts and their real parts symmetrical on either side of $\omega t=\pi$.

For elliptical polarization, the location of the SPs in the complex plane depends upon whether the discriminant D is positive or negative. For $D>0$, we have the same situation as for linear polarization. However, for $D\leqslant 0$, $\cos(\omega t)$ on the right-hand side of (10) is real so that we have the two solutions

$$(\omega t_\mathrm{R})_{1,2}=\pi,\quad (\omega t_\mathrm{I})_{1,2}=\operatorname{arcosh}\left(\frac{\epsilon\pm\sqrt{-D}}{\zeta\sqrt{1+\xi^2}}\right), \tag{11}$$

which have the same real parts and differ by their imaginary parts. Here $\operatorname{arcosh}(z)=\ln(z+\sqrt{z^2-1})$. For $D=0$ we have a double root.

In figure 1 we compare the differential detachment rate (4) obtained by numerical integration and using the relations (7) and (A.4) with the one obtained using the SP method, relation (A.5). Below the critical point, for which the discriminant D is equal to zero, we take into account the two complex SP solutions t_1 and t_2 in the upper half complex plane, which are determined by (10) for $D>0$. For the ellipticity $\xi=0.5$, which underlies figure 1, the critical electron energy, determined by the condition $D=0$, is $E_{\mathbf{p},\mathrm{c}}=1.62U_\mathrm{p}$. For $E_\mathbf{p}<1.62U_\mathrm{p}$ two SP contributions interfere and the resulting spectrum agrees very well with the exact spectrum obtained by numerical integration in relation (A.4). With $E_\mathbf{p}$ approaching $1.62U_\mathrm{p}$ this agreement becomes worse and for $E_\mathbf{p}=1.62U_\mathrm{p}$ the SP approximation exhibits an artificial spike. For $E_\mathbf{p}>1.62U_\mathrm{p}$ we separately present the spectra obtained using the contributions of the solutions t_1 and t_2. The contribution of the solution t_2 starts from the afore-mentioned spike, but for $E_\mathbf{p}>E_{\mathbf{p},\mathrm{c}}$, the agreement with the exact result is becoming better again. On the other hand, the contribution of the solution t_1 increases for $E_\mathbf{p}>E_{\mathbf{p},\mathrm{c}}$ and diverges upon further increase of $E_\mathbf{p}$. From the inset of figure 1 we see that for $E_\mathbf{p}\geqslant E_{\mathbf{p},\mathrm{c}}$ the real parts of the solutions t_1 and t_2 are equal to π/ω while their imaginary parts are such that $\mathrm{Im}\,t_2<\mathrm{Im}\,t_1$ and $\mathrm{Im}\,t_1$ increases while $\mathrm{Im}\,t_2$ decreases with increasing $E_\mathbf{p}$, see (11). If for $E_\mathbf{p}\geqslant E_{\mathbf{p},\mathrm{c}}$ the contour of integration in the complex plane is deformed such that it passes only through the SP that is nearest the real axis (i.e. the SP t_2), then the agreement of the SP result and the exact numerical result is very good except in the region of the spike near $E_{\mathbf{p},\mathrm{c}}$. The physical interpretation of this result in [21, 22] was given in terms of the tunnelling time: the real part of the time t is attributed to the time at which the electron 'leaves the tunnel'. For $E_\mathbf{p}<E_{\mathbf{p},\mathrm{c}}$, there are two such times per cycle and their contributions interfere. For $E_\mathbf{p}>E_{\mathbf{p},\mathrm{c}}$, there is only one such time and, correspondingly, no interference. This theoretical interpretation is in agreement with the measured photoelectron ATI spectra [21, 22].

Let us now consider the choice of the integration contour more carefully [23]. We first consider the case $E_\mathbf{p}=1.3U_\mathrm{p}<E_{\mathbf{p},\mathrm{c}}$ where both SP solutions should be taken into account.

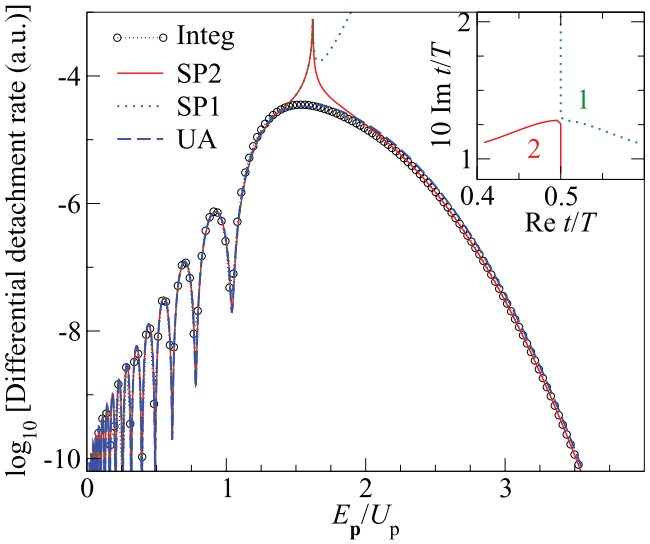

Figure 1. Differential detachment rate of the F^- ion by an elliptically polarized laser field as a function of the photoelectron kinetic energy $E_{\mathbf{p}}$ (in units of the ponderomotive energy U_p) for the electron emission angle $\theta = 0°$ (in the direction of the large component of the laser field). The laser-field ellipticity is $\xi = 0.5$, the intensity is 8×10^{13} W cm^{-2} and the wavelength is 1800 nm. The results obtained using the strong-field approximation and numerical integration are presented by the black dotted line with circles. The spectra obtained using the SP method taking into account both solutions below the critical point and only the solution 1 (2) after this point are denoted by SP1 (SP2). The results obtained using the uniform approximation are presented by the blue dashed line and denoted by UA. The inset in the upper right corner shows the SP solutions t_1 (dark green dotted line) and t_2 (red solid line) in the complex plane for the electron energies $U_p < E_{\mathbf{p}} < 2.2U_p$.

In the entire complex time plane there are four SP solutions: t_1 and t_2 ($t_3 = t_1^*$ and $t_4 = t_2^*$) are in the upper (lower) half plane. Introducing the quantity $\Phi(t) = S(\mathbf{p}; t)\omega/U_p$ we consider the factors $\mathrm{Im}\,(\mathrm{i}\Phi)$ and $\mathrm{Re}\,(\mathrm{i}\Phi)$, which appear in the exponent of the integral (1). The 'steepest descent' integration path should be chosen so that $\mathrm{Im}\,(\mathrm{i}\Phi(t)) = \mathrm{Im}\,(\mathrm{i}\Phi(t_s)) = \mathrm{const}$ in order to quench the otherwise rapid oscillations along the path. These lines in the complex time plane are shown in figure 2: the blue dot-dashed lines run through the SPs t_1 (white circle) and t_3 (black circle) while the red solid lines run through t_2 (white circle) and t_4 (black circle). In addition, in the contour plot the value of $R \equiv \mathrm{Re}\,(\mathrm{i}\Phi(t))$ is indicated by the blue-yellow color scale. A bright (yellow) shade means a large real part of the exponent. Thus the integrand diverges in the brightest (yellow) areas and vanishes in the darkest (blue) areas. (Since $|R| \gg 1$ in parts of the complex plane, we use a logarithmic scale; more precisely, we present $\mathrm{sign}(R)\log_{10}(|R|/\min_t(|R|))$). The integration contour goes from $t = 0$ to its upper limit at $\omega t = 2\pi$. The steepest-descent method calls for the contour to stay in regions as dark (blue) as possible so that it collects its dominant contributions from the vicinity of the SPs at which R is maximal, all the while maintaining $\mathrm{Im}\,(\mathrm{i}\Phi(t)) = \mathrm{const}$ [13, 14]. This excludes routing the path through the SPs t_3 and t_4 in the lower half complex plane. Therefore, there is exactly one possible integration path (denoted by the bold lines for visual convenience): from $t = 0$ to $\mathrm{i}\infty$, then along the blue dot-dashed line over the first saddle point (left white circle) to $\omega t = \pi + \mathrm{i}\infty$, subsequently via the second saddle point (right white circle) to $\omega t = 2\pi + \mathrm{i}\infty$, and finally along the imaginary axis to $\omega t = 2\pi$. The two integrals along the imaginary axis

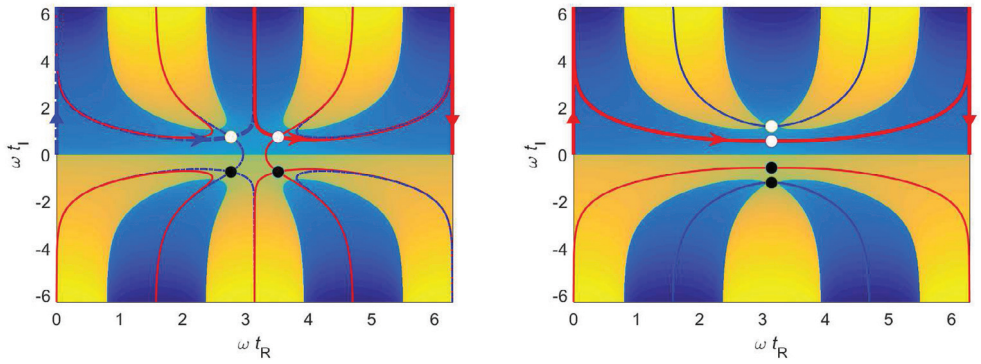

Figure 2. Choice of the integration contour for constant imaginary part of the exponent $\mathrm{i}\Phi(t)$. The arrows and bold lines mark the only possible integration contour. In the left panel, the energy $E_{\mathbf{p}} = 1.3U_{\mathrm{p}} < E_{\mathbf{p},\mathrm{c}}$ is below the critical value; the two SPs have the same imaginary part and the contour in the upper half plane runs over both of them; in the right panel, where $E_{\mathbf{p}} = 2U_{\mathrm{p}} > E_{\mathbf{p},\mathrm{c}}$, the two SPs lie on top of each other, and the contour runs over the one with the smaller imaginary part bypassing the other one. The blue dot-dashed curves indicate contours with $\mathrm{Im}\,(\mathrm{i}\Phi(t)) = \mathrm{Im}\,(\mathrm{i}\Phi(t_{1,3}))$, the red solid ones with $\mathrm{Im}\,(\mathrm{i}\Phi(t)) = \mathrm{Im}\,(\mathrm{i}\Phi(t_{2,4}))$. The blue and yellow scales represent the magnitude of the real part of the exponent. Dark blue shading stands for small real parts, light yellow for large real parts. The color scale is logarithmic. The other parameters parameters are as in figure 1.

for $\omega t = 0$ and $\omega t = 2\pi$ cancel each other (their magnitudes are identical and, because of the reversed boundaries, they add to zero). Therefore, only the sections of the contour contribute that run through the SPs t_1 and t_3. They are approximated by the sum of two SP contributions (6). As we have seen, for $E_{\mathbf{p}} < E_{\mathbf{p},\mathrm{c}}$ this approximation agrees very well with the exact result.

For $E_{\mathbf{p}} > E_{\mathbf{p},\mathrm{c}}$ the shape and topology of the contour in the complex time plane change. This is illustrated in the right panel of figure 2 for $E_{\mathbf{p}} = 2U_{\mathrm{p}}$. The integration extends via the SP t_2 (lower white circle) with the lower but positive imaginary part. Taking into account only the SP t_2 leads to a good agreement with the exact result for $E_{\mathbf{p}} > E_{\mathbf{p},\mathrm{c}}$. Note that there is no way to deform the contour so that it passes through both SPs while $\mathrm{Im}\,(\mathrm{i}\Phi(t)) = \mathrm{Im}\,(\mathrm{i}\Phi(t_s)) = \mathrm{const}$.

For $E_{\mathbf{p}} \approx E_{\mathbf{p},\mathrm{c}}$ the SPs very closely approach each other. In this case, neither the expansion of the exponent in the integrand up to the second order, as it is done in the standard SP method, nor treating the two SPs as independent is justified. In this case a uniform approximation [24, 25] has to be used in place of the standard SP (steepest descent) approximation. The results obtained using the uniform approximation of [26] are represented in figure 1 by the blue dashed line. The agreement with the exact result is excellent, even in the region near $E_{\mathbf{p}} = 1.62U_{\mathrm{p}}$ where the SP approximation produces a spike. Other examples of the use of the uniform approximation in strong-field physics can be found in [26–28]. The case of three SPs in close proximity is more complicated, but the corresponding approximate methods can be found in [24]. As far as we know, in strong-field physics such a case appeared in high-order ATI where one backward and two forward scattering solutions approach each other [29].

The change of the topology of the SP solutions as a function of some parameter is ubiquitous in problems involving rescattering where it always happens at a cutoff in energy where two solutions approach each other and almost merge, see e.g. [4, 7], but it is rare for direct electrons.

4. Number of solutions of the saddle-point equation

We want to determine the number of solutions of the SP equation $S'(\mathbf{p};t_s)=0$ for the ionization time. According to (2), this equation has the form

$$\frac{1}{2}\left[\mathbf{p}+\mathbf{A}(t)\right]^2=-I_\mathrm{p}, \tag{12}$$

where the ionization potential I_p is a positive number and the photoelectron momentum $\mathbf{p}$ is a real vector. Since electromagnetic waves are transverse, the vector $\mathbf{A}(t)$ is defined in a plane (say the xy plane), so that, for the real time t, it is defined by two real numbers, viz. the components $A_x(t)$ and $A_y(t)$. One usually considers the electrons emitted in the laser-field polarization plane, determined by the real components $p_x=p\cos\theta$ and $p_y=p\sin\theta$, where $p=|\mathbf{p}|$ and θ is the electron emission angle with respect to the x axis. Since $-I_\mathrm{p}<0$, equation (12) has solutions only for complex times t. The vector potential of the laser field is a 2π-periodic function of the parameter $\varphi=\omega t$ which means that $\mathbf{A}(t+jT)=\mathbf{A}(t)$, with j integer and $T=2\pi/\omega$ the period of the laser field. For an arbitrary polychromatic elliptically polarized laser field with frequencies equal to integer multiples of the fundamental frequency ω, (12) can be rewritten as $f(\varphi)=0$ where $f(\varphi)$ is a trigonometric polynomial of nth order

$$f(\varphi)=\sum_{k=0}^{n}a_k\cos(k\varphi)+\sum_{k=1}^{n}b_k\sin(k\varphi), \tag{13}$$

with real coefficients a_k and b_k. Introducing the variable $z=\mathrm{e}^{\mathrm{i}\varphi}$ and using the relations

$$\cos(k\varphi)=\frac{z^k+z^{-k}}{2},\quad \sin(k\varphi)=\frac{z^k-z^{-k}}{2\mathrm{i}}, \tag{14}$$

we rewrite (13) as $f(\varphi)=\mathrm{e}^{-\mathrm{i}n\varphi}F(\mathrm{e}^{\mathrm{i}\varphi})$ where

$$F(z)=a_0z^n+\sum_{k=1}^{n}\left[\frac{a_k}{2}\left(z^{n+k}+z^{n-k}\right)+\frac{b_k}{2\mathrm{i}}\left(z^{n+k}-z^{n-k}\right)\right]. \tag{15}$$

With the substitutions $l=n+k$ (for the terms with the factor z^{n+k}) and $m=n-k$ (for the terms with the factor z^{n-k}) we obtain

$$F(z)=a_0z^n+\sum_{m=0}^{n-1}c_mz^m+\sum_{l=n+1}^{2n}c_{2n-l}z^l \tag{16}$$

with

$$c_k=c_{2n-k}^*=\frac{a_{n-k}+\mathrm{i}b_{n-k}}{2},\quad k=0,1,2,\ldots,n-1. \tag{17}$$

Denoting also $c_n=a_0$ we rewrite $F(z)$ as the following polynomial of order $2n$

$$F(z)=\sum_{k=0}^{2n}c_kz^k \tag{18}$$

which has exactly $2n$ zeros $z_1,\ldots,z_{2n}$ provided $c_{2n}\neq 0$. The corresponding zeros of the trigonometric polynomial $f(\varphi)$ are

$$\varphi_k=-\mathrm{i}\ln z_k,\quad 0\leqslant\mathrm{Re}\,\varphi_k<2\pi,\quad k=1,2,\ldots,2n. \tag{19}$$

Our final result is that the trigonometric polynomial (13) of the nth order, with real coefficients a_k, b_k, such that a_n and b_n are not simultaneously equal to zero, has exactly $2n$ zeros, i.e. $2n$ complex solutions φ, $0 \leqslant \mathrm{Re}\,\varphi < 2\pi$. Since the coefficients a_k and b_k are real, for any solution $\varphi_s = \omega t_s$ its complex conjugate $\varphi_s^* = \omega t_s^*$ is another solution. In applications, the steepest-descent method requires that we take into account the n solutions in the upper half complex plane. In the examples, to be presented in the next section, we will find all solutions of the relevant SP equation using standard methods of numerical analysis. One equation for the complex time can be expressed as a system of two real equations for two real unknowns: the real and the imaginary parts of the complex time t. This system can be solved using the subroutine ZSPOW from the International Mathematics and Statistics Library (IMSL). The computational time is very short (a few seconds on a typical PC) and is comparable with that of the conventional saddle-point method.

5. Examples of tailored fields

5.1. Bicircular field

A bicircular laser field is a special case of a bichromatic field with two coplanar counter-rotating circularly polarized components. It is particularly interesting since it can serve as a source of circularly polarized soft x rays emitted in laser-field-induced high-order harmonic generation. High harmonics generated by a bicircular field were observed in 1995 [30] and the process was modeled using a zero-range atomic binding potential [31] and quantum-orbit theory [32]. The circular polarization of the high-order harmonics was confirmed in the experiment [33] which revived the exploration of this process (see, for example [34–36], and references therein). Strong-field ionization, the process we are considering in the present paper, by such a field was first considered in [37, 38]. For more recent results see [20, 39] and references therein. We consider a bicircular field with the components having intensities I_1 and I_2 and angular frequencies $r\omega$ and $s\omega$, where r and s are integers and $\omega = 2\pi/T$ is the fundamental frequency. The components of the corresponding vector potential, defined in the xy plane, are

$$A_x(t) = \frac{1}{\sqrt{2}}\left[A_1\cos(r\omega t) + A_2\cos(s\omega t)\right], \quad A_y(t) = \frac{1}{\sqrt{2}}\left[A_1\sin(r\omega t) - A_2\sin(s\omega t)\right], \tag{20}$$

where $A_1 = E_1/(r\omega)$, $E_1 = \sqrt{I_1}$, $A_2 = E_2/(s\omega)$, $E_2 = \sqrt{I_2}$ and

$$\mathbf{A}^2(t) = 2U_\mathrm{p} + A_1A_2\cos((r+s)\omega t), \quad U_\mathrm{p} = \frac{1}{4}(A_1^2 + A_2^2), \tag{21}$$

with U_p the ponderomotive energy. Introducing (20) and (21) into (12) and comparing with (13) we conclude that for the bicircular field we have $n = r + s$ so that the SP equation (12) has $2(r + s)$ solutions of which the $r + s$ solutions in the upper half complex time plane should be taken into account.

The bicircular-field vector potential is invariant with respect to a rotation by the angle $360^\circ/(r + s)$. It also obeys reflection symmetries about axes at the angle $180^\circ/(r + s)$ as well as integer multiples of this angle, with respect to the positive A_x axis. Examples are exhibited in the right-hand part of figure 4 and in the upper right corner of the upper left panel of figure 5.

We will first consider the simplest example of the bicircular field with $r = 1$ and $s = 2$. Figure 3 displays the corresponding spectra for emission in the direction $\theta = 0^\circ$. We compare the case where the two field components have equal intensities ($I_1 = I_2 = 4 \times 10^{13}$ W cm^{-2}) (left panel) with the case of almost circular polarization (I_1

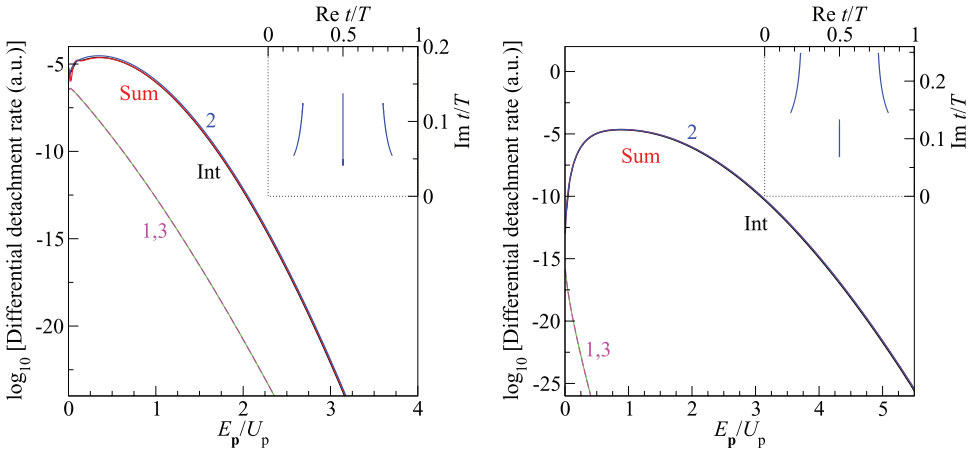

Figure 3. Energy spectrum (in multiples of U_{p}) in the direction $\theta = 0°$ for ionization of the F^- ion by a bicircular $(r = 1, s = 2)$ field with wavelength 1800 nm and equal component intensities $I_1 = 4 \times 10^{13}$ W cm^{-2} and $I_2 = I_1$ (left panel) and the close-to-circular case where $I_2 = 0.13 \times 10^{13}$ W cm^{-2} (right panel). In either case, the SP solutions are presented in the upper right corners. In the text, they are numbered by $1, 2, 3$ from left to right. The curves display the results of numerical integration ('Int'), the SP approximation with all SPs ('sum'), the SP solutions 1 and 3 ('1,3') and only solution 2 ('2').

as before, $I_2 = 0.13 \times 10^{13}$ W cm$^{-2} \ll I_1$). In either case, there are three SP solutions in the upper half plane, which are presented in the insets, as well as their complex conjugates in the lower half plane. One solution (solution 2) has $\mathrm{Re}\, t = T/2$ and the other two (solutions 1 and 3) are located symmetrically on either side of the former. For either intensity ratio, the solution 2 is completely dominant. Indeed, the two panels show that the exact result (denoted by 'Int') is indiscernible from the contribution of only the SP 2 (denoted by '2'). For the close-to-circular case the contribution of the SP pair (1,3) is suppressed by a huge factor, in agreement with the fact that the imaginary parts of the solutions $t_{1,3}$ are very much larger.

In analogy with figures 2 and 4 illustrates how the contour of integration has to be deformed so that is runs over the relevant SPs. For $I_1 = I_2$, these are indicated by the white filled circles in the upper half plane. As in the case of figure 2, the complex conjugate SPs, which are denoted by the black filled circles, cannot be accessed by a contour that satisfies all requirements. We concluded above that the SP 2 with $\mathrm{Im}\, t_2 = T/2$ is completely dominant. The reason is that its imaginary part is much smaller than that of the other two SPs 1 and 3 (owing to the scale of figure 4, this is difficult to see in the figure). The red squares in figure 4 denote the SPs for the near-circular case. Here, the disparity of the imaginary parts between solution 2 and solutions 1 and 3 is much larger and very evident in the figure. The color coding of figure 4 corresponds to the case $I_1 = I_2$. For $I_1 \gg I_2$, the yellow (light) areas in the upper half plane will move to larger values of ωt_{I} so that the red squared SPs will come to lie in the blue (dark) area. Therefore, the contour of integration will stay in the blue (dark) area and run over all three SPs. The main message of this discussion is that for a bicircular field, in contrast to elliptical polarization considered in section 3, the topology of the SP solutions and the integration contour in the complex plane are independent of the parameters (here the intensity ratio).

As another example, we consider the case $r = 3$, $s = 5$. We only discuss the SP solutions and take it for granted, on the basis of the previous investigation of the case $r = 1$ and $s = 2$,

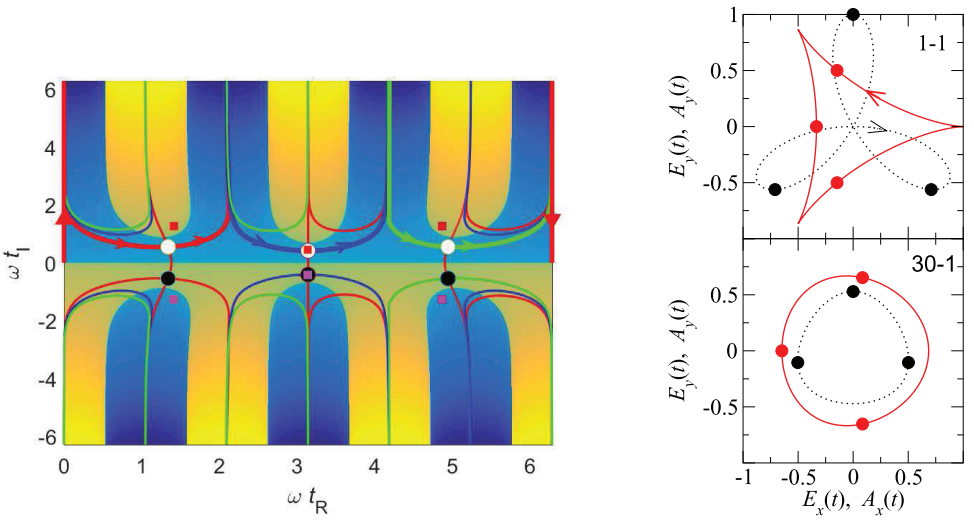

Figure 4. Left panel: analog of figure 2 for the bicircular field with $r = 1$ and $s = 2$. The parameters are the same as in figure 3. The SPs are indicated by white (black) filled circles in the upper (lower) half plane for the case where $I_1 = I_2$ and by red filled squares for $I_1 \gg I_2$. The color code is for the case $I_1 = I_2$; the case $I_1 \gg I_2$ is not presented. Right panels: parametric plots of the vector potential (equation (20); red solid line) and the electric field (black dotted line) for $I_1 = I_2$ (upper panel) and $I_1 \gg I_2$ (lower panel) for $0 \leqslant t \leqslant T$. The values of $\mathbf{A}(\mathrm{Re}\, ts)$ and $\mathbf{E}(\mathrm{Re}\, ts)$ are represented by the filled circles on the curves. For either set of field parameters, $\mathbf{A}(\mathrm{Re}\, t_s)$ for the dominant solution $s = 2$ is located on the negative horizontal axis, while $\mathbf{A}(\mathrm{Re}\, t_s)$ for the solutions $s = 1$ and $s = 3$ are located symmetrically on either side of the horizontal axis. In the limit of purely circular polarization, the curves of the lower panel turn into circles.

that the integration contour will pick up all SPs in the upper half plane. The field is sketched in the inset in the upper left panel of figure 5. In view of the rotation and reflection symmetries discussed above, for the 3ω–5ω bicircular laser field it is sufficient to analyse the spectra for the electron emission angle $\theta \in [0, 22.5°]$. It should be mentioned that the 3ω–5ω field was utilized in the experiment in which bright circularly polarized soft x-ray high harmonics were used for x-ray magnetic circular dichroism [35, 39].

In figure 5 we present spectra for the angles $\theta = 0°, 11.25°$ and $22.5°$. We notice that the results for these angles are qualitatively different. For $\theta = 0°$, the rates for the electron energies $E_\mathbf{p} > 1.1U_\mathrm{p}$ are much larger than for the other two cases. For $\theta = 22.5°$ the spectrum exhibits very rapid oscillations. This behaviour can be explained using the SP method. Let us first consider the $\theta = 0°$ case (lower right panel). The $r + s = 8$ SP solutions for the complex time are presented in the upper right part of this panel. The corresponding photoelectron energy is $0 < E_\mathbf{p} < 4U_\mathrm{p}$, with, generally, $E_\mathbf{p} = 0$ at the bottom (smallest $\mathrm{Im}\, t$) and $E_\mathbf{p} = 4U_\mathrm{p}$ at the top of each trace (largest $\mathrm{Im}\, t$). These solutions are symmetric with respect to the $\mathrm{Re}\, t = 0.5T$ line, i.e. they come in pairs $(1, 8)$, $(2, 7)$, $(3, 6)$ and $(4, 5)$. The pair $(4, 5)$ in the middle makes the dominant contribution. The interference of the contributions of this pair is responsible for the oscillations in the spectrum for energies larger than $1U_\mathrm{p}$, especially for the deep suppression at about $1.16U_\mathrm{p}$. For lower energies the pair $(2, 7)$ also contributes and the interference picture due to the four SP solutions is more complicated. The inset in the lower right panel of figure 5 shows that indeed the pairs (4,5) and (2,7) have the smallest imaginary parts of the ionization time. For the angle $\theta = 11.25°$ all eight solutions contribute leading to the spectra

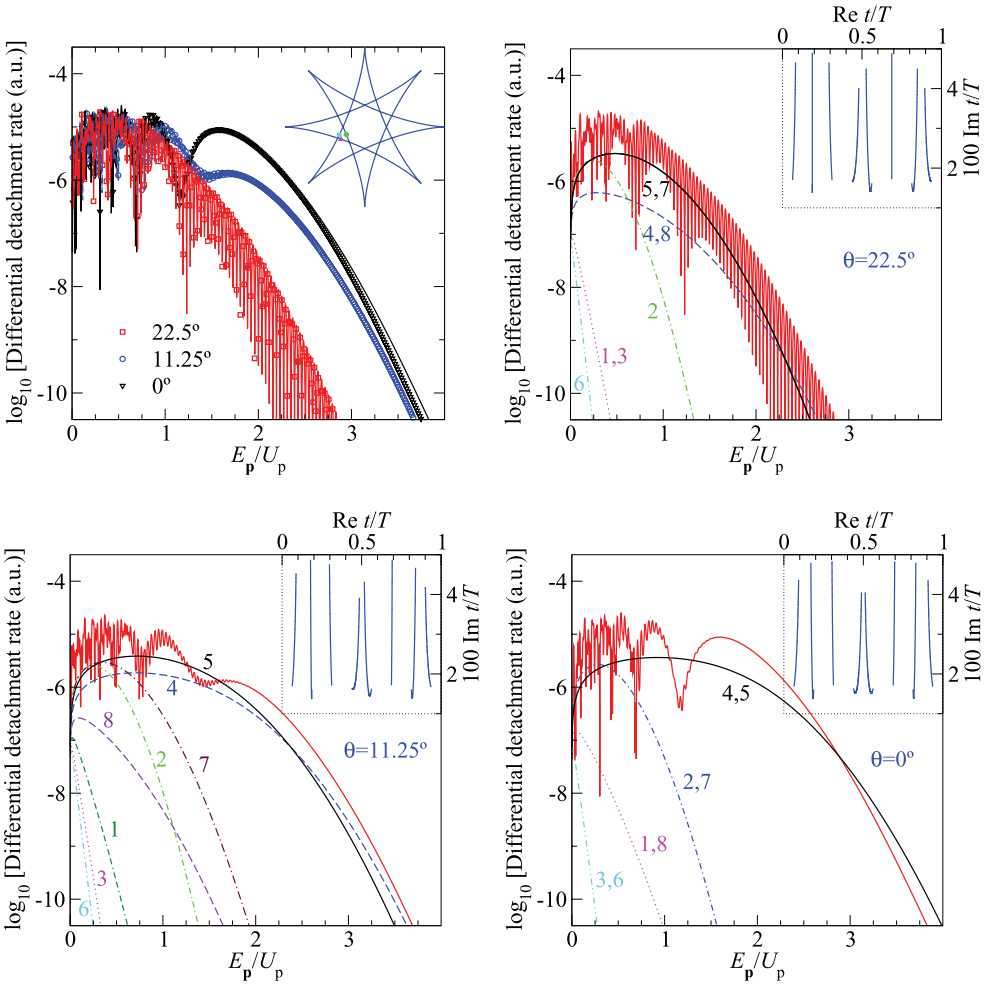

Figure 5. Differential detachment rates of the F^- ion by the 3ω–5ω bicircular laser field as functions of the photoelectron kinetic energy $E_\mathbf{p}$ (in units of U_p) for the electron emission angles $\theta = 0°$, $11.25°$ and $22.5°$, as denoted in the legend. Component intensities and wavelengths are $I_1 = I_2 = 4 \times 10^{13}$ W cm^{-2} and 1800 nm (3ω) and 1080 nm (5ω). Upper left panel: the spectra obtained using the SFA and numerical integration are represented by symbols. The corresponding spectra obtained using the SP method are denoted by lines. In the upper right corner of this panel the polar diagram of the vector potential $\mathbf{A}(t)$ is presented. The symbols denote the values of $\mathbf{A}(\mathrm{Re}\, t_s)$ for $\theta = 22.5°$, $E_\mathbf{p} = 0.2U_\mathrm{p}$ and $s = 2$ (green circle), 5 (magenta triangle) and 7 (cyan square). In the remaining panels, denoted by the corresponding angle θ, the spectra obtained using the SP method are exhibited. The partial contributions of each of the eight SP solutions t_s are identified by the numbers $1, 2, \ldots, 8$. In the upper right corner of each panel the solutions t_s, $s = 1, 2, \ldots, 8$ (from left to right) are presented in the complex time plane, for $0 < E_\mathbf{p} < 4U_\mathrm{p}$.

shown in the lower left panel. The contributions of the solutions 4 and 5 are again dominant. However, their partial rates are not equal, as was the case for $\theta = 0°$, so that the interference minima and maxima are less pronounced. For the angle $\theta = 22.5°$ (upper right panel), the two pairs of solutions, $(5, 7)$ and $(4, 8)$, make comparable contributions in the high-energy

region, which leads to the wild oscillation in this part of the spectrum. In addition, for low energies the solution 2 is significant. Indeed, looking at the parametric plot of $\mathbf{A}(t)$ in the upper right corner of figure 5 and recalling that direct electrons are roughly emitted in directions compatible with $\mathbf{p} = -\mathbf{A}(t)$ one will notice a small triangle formed by $\mathbf{A}(t)$ around the angle $-\theta = -22.5°$, which consists of three different small segments of the curve $\mathbf{A}(t)$. The real parts of the afore-mentioned SP solutions 2 (green circle), 5 (magenta triangle) and 7 (cyan square) lie on these segments (they correspond to the energy $E_{\mathbf{p}} = 0.2U_{\mathrm{p}}$). The SP-method results described above agree very well with the results obtained by numerical integration, which are displayed by the symbols in the upper left panel. Small differences appear only for the high-energy part of the spectra for the angle $\theta = 0°$. The advantage of the SP method is that one can explain the behaviour of the obtained spectra in terms of the partial contributions of particular SP solutions and their interference. Hence, one can infer with attosecond precision at which times electrons that make up a certain part of the spectrum have been released.

5.2. Few-cycle linearly polarized laser pulse

The electric-field vector and the vector potential of a linearly polarized few-cycle laser pulse with a sine-squared envelope and the carrier-envelope phase ϕ are defined by [7, 40, 41]

$$\mathbf{E}(t) = \hat{\mathbf{e}}_x E_0 \sin^2\left(\frac{\omega_{\mathrm{p}} t}{2}\right)\cos(\omega t + \phi) = \hat{\mathbf{e}}_x \sum_{j=0,1,2} \mathcal{E}_j \cos(\omega_j t + \phi), \tag{22}$$

$$\mathbf{A}(t) = -\hat{\mathbf{e}}_x \sum_{j=0,1,2} \frac{\mathcal{E}_j}{\omega_j}\sin(\omega_j t + \phi), \tag{23}$$

where $\mathcal{E}_0 = E_0/2$, $\mathcal{E}_j = -\mathcal{E}_0/2$ $(j = 1, 2)$, $\omega_{\mathrm{p}} = \omega/n_{\mathrm{p}}$, $\omega_0 = \omega$, $\omega_{1,2} = \omega \pm \omega_{\mathrm{p}}$. We assume that the pulse duration during which the electric field is different from zero is an integer number n_{p} of optical cycles, $T_{\mathrm{p}} = n_{\mathrm{p}} T$. The field (22) is trichromatic comprising the frequencies ω and $\omega \pm \omega_{\mathrm{p}}$. The above-described theory can also be applied to this field assuming that the fundamental frequency is ω_{p} (instead of ω). In this case, the vector potential is expressed as a linear combination of sine functions with the arguments $n_{\mathrm{p}}\varphi$ and $(n_{\mathrm{p}} \pm 1)\varphi$, where now $\varphi = \omega_{\mathrm{p}} t$. Introducing this into (12), after some trigonometric transformations, independently of the value of the carrier-envelope phase ϕ, we obtain a trigonometric polynomial of the order $n = 2(n_{\mathrm{p}} + 1)$. Therefore, the SP equation (12) for our few-cycle linearly polarized laser pulse with sine-squared envelope has $4(n_{\mathrm{p}} + 1)$ solutions of which we take the $2(n_{\mathrm{p}} + 1)$ solutions in the upper half of the complex time plane. Examples of these solutions can be found in section 6 of [7] (see figures 12 and 13 therein; see also the more recent paper [42] and references therein).

5.3. Orthogonally polarized two-color laser field

In this section we consider the number of SP solutions for an orthogonally polarized bichromatic laser field. The field is a superposition of two mutually orthogonal linearly polarized laser fields with frequency $r\omega$ and $s\omega$, with r and s integers. According to our knowledge, first experiments with ω–2ω and ω–3ω OTC fields were reported in [43] and [44], respectively. For more references, see the recent work [45]. The electric-field vector $\mathbf{E}(t)$ and the corresponding vector potential $\mathbf{A}(t)$ of the OTC field can be written as

$$\mathbf{E}(t) = E_1 \sin(r\omega t)\hat{\mathbf{e}}_x + E_2 \sin(s\omega t + \phi)\hat{\mathbf{e}}_y, \quad \mathbf{A}(t) = A_1 \cos(r\omega t)\hat{\mathbf{e}}_x + A_2 \cos(s\omega t + \phi)\hat{\mathbf{e}}_y, \tag{24}$$

where $E_1 = \sqrt{I_1}$, $A_1 = E_1/(r\omega)$, $E_2 = \sqrt{I_2}$, $A_2 = E_2/(s\omega)$ and ϕ is the relative phase between the two orthogonal components. It is straightforward to show that, for such a field, equation (12) reduces to

$$\frac{A_1^2}{4}\cos(2r\omega t) + \frac{A_2^2}{4}\cos(2s\omega t + 2\phi) + A_1 p_x \cos(r\omega t) + A_2 p_y \cos(s\omega t + \phi) + U_\mathrm{p} + E_\mathbf{p} = -I_\mathrm{p}, \tag{25}$$

where $U_\mathrm{p} = (A_1^2 + A_2^2)/4$ is the ponderomotive energy and $E_\mathbf{p} = \mathbf{p}^2/2$ the electron kinetic energy. Using trigonometric addition formulas the relation (25) can be rewritten in the form (13) with $n = 2s$ and $s > r$. Therefore the number of SP solutions in the upper half of the complex plane is $2s$.

Let us consider ATI of neon atoms by an OTC field and analyse the results. In figure 6 we present the differential ionization rates of Ne by the ω–3ω (upper panels) and ω–4ω (lower panels) OTC field as a function of the photoelectron kinetic energy $E_\mathbf{p}$. Ionization rates are obtained for two values of the relative phase: $\phi = 90°$ (left panels) and $\phi = 180°$ (right panels), electron emission at the angle $\theta = 15°$ and laser-field parameters as stated in the caption. In the upper left corner of each panel, a polar diagram of the vector potential $\mathbf{A}(t)$ for $0 \leqslant t \leqslant T$ is shown, while in the upper right corners we present the SP solutions in the complex plane.

For the ω–3ω field, we find, as expected, six SP solutions. Three of them, namely the solutions denoted by 3, 4 and 5 significantly contribute to the spectra for $\phi = 90°$ (upper left panel), while the other three SPs can be neglected (their contributions are more than five orders of magnitude lower and are not shown in the panel; the corresponding imaginary parts of the complex ionization time for these three solutions are much larger in comparison with the other three solutions, so that the corresponding tunnelling probability is negligible). The solutions denoted by 3 and 5 interfere for energies below $1U_\mathrm{p}$, which results in the oscillations visible in this region of the spectrum. A destructive interference of the contributions 3 and 4 is responsible for the pronounced dip in the spectrum at energies about $1.5U_\mathrm{p}$. For energies higher than $1.5U_\mathrm{p}$ only one solution, denoted by 4, contributes to the spectrum.

If we change the phase between the two orthogonal field components from $\phi = 90°$ to $\phi = 180°$, the partial contributions as well as the overall spectrum change significantly. With increasing ϕ the partial contributions shift to the right (i.e. to larger values of $\mathrm{Re}\, t$), but the contributions of the solutions 2, 3, 4 and 5 remain dominant. For $\phi = 180°$ the solutions become symmetric with respect to the line $\mathrm{Re}\, t = 0.5T$, and they come in three pairs denoted by $(1, 6)$, $(2, 5)$ and $(3, 4)$ so that the two members of each pair make identical contributions. For energies lower than $0.5U_\mathrm{p}$ only the pair $(2, 5)$ contributes to the spectrum and is responsible for its oscillatory character. For higher energies the pair $(3, 4)$ alone is sufficient to reproduce the overall spectrum. These observations are nicely reproduced by the plots of the complex ionization times displayed in the inset of the upper right panel of figure 6. Namely, for small energies the solutions (2,5) are dominant (having the smallest imaginary parts) while for larger energies the pair (3,4) takes over (as a function of the energy, its imaginary parts start at large values, assume a minumum around $E_\mathbf{p} = 1.2U_\mathrm{p}$ and then increase again). Since the absolute values of the ionization amplitudes of the two members of each pair are equal, these amplitudes interfere constructively or destructively, depending on the electron energy, and therefore we notice more pronounced oscillations in the ATI spectrum for the phase $\phi = 180°$ compared with the phase $\phi = 90°$.

For an ω–4ω OTC field, we numerically find eight SP solutions of equation (12), in accordance with our analytical findings. These solutions, as well as their partial contributions, are shown in the lower panels of figure 6. The solutions 3, 4 and 7 reproduce the low-energy part of the spectrum for $\phi = 90°$ (lower left panel), while the solutions 4, 5 and 6 are dominant

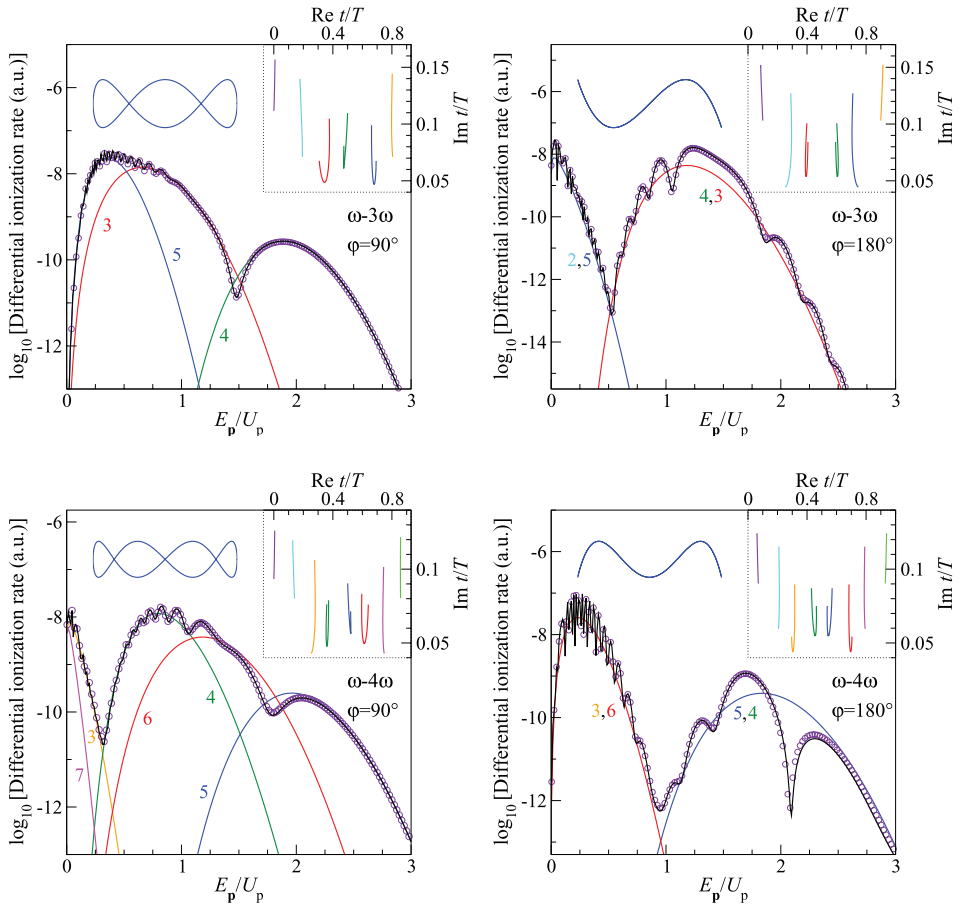

Figure 6. Differential ionization rates of neon by the ω–3ω (upper panels) and ω–4ω (lower panels) OTC field as a function of the photoelectron kinetic energy $E_{\mathbf{p}}$ (in units of the ponderomotive energy U_{p}) for the relative phase $\phi = 90°$ (left panels) and $\phi = 180°$ (right panels) and electron emission angles $\theta = 15°$. The laser-field component intensities are $I_1 = I_2 = 2 \times 10^{14}$ W cm^{-2}, while the fundamental wavelength is 1800 nm. We present the relevant partial contributions of each SP solution and the corresponding spectra obtained by the SP method (black solid line) and numerical integration (violet circles). Some of the partial contributions, whose yields are more than five orders of magnitude lower than the overall yield, are not shown in the panels. In the upper left corner of each panel we present a polar diagram of the respective vector potential $\mathbf{A}(t)$, plotted for $0 \leqslant t \leqslant T$, while in the upper right corners we display in the complex time plane the SP solutions for energies from 0 to $5U_{\mathrm{p}}$.

in the energy range above $0.5U_{\mathrm{p}}$. The contributions of the other three solutions are negligible and are not shown. By changing the phase from $\phi = 90°$ to $\phi = 180°$ the SP solutions become symmetric with respect to the line $\mathrm{Re}\, t = 0.5T$, similarly to the case of the ω–3ω OTC field. For energies below $1U_{\mathrm{p}}$ the pair (3,6) dominates the spectrum; above $1U_{\mathrm{p}}$ the pair (4,5) takes over. Like above, these observations are reflected in the imaginary parts of the ionization time. The corresponding interference patterns, where the oscillations are more closely spaced when the SP solutions are farther apart, are clearly visible in the spectrum. We note that the

SP spectra agree very well with the results of the numerical integration, which are presented by circles in each panel of figure 6.

6. Conclusions

Quantum-mechanical transition amplitudes of atomic and molecular processes induced by strong laser fields are typically expressed in the form of integrals of highly oscillatory functions. Using the SP method such an integral is approximated by a sum over the solutions of the SP equation for the complex ionization time. For an arbitrarily polarized polychromatic laser field the solutions of the SP equation can be found as zeros of a trigonometric polynomial of the nth order. It is shown that such a polynomial has exactly $2n$ zeros—complex solutions for the ionization time within one optical cycle. For applications, the n solutions in the upper half complex time plane are relevant.

For some critical values of the atomic and photoelectron parameters and the laser field parameters the number of relevant SP solutions can be smaller. This can happen if two SP solutions approach each other so that the topology of the 'steepest descent' integration contour changes. In this case the contribution of the solution having the larger imaginary part of the ionization time should be neglected. Close to these critical values, the uniform approximation, which takes into account both solutions, should be used instead of the SP approximation. We used the example of an elliptically polarized monochromatic laser field to illustrate how the afore-mentioned topology changes for some critical value of the photoelectron energy and how the uniform approximation is used close to this critical point.

In most applications, it is sufficient just to insert the solutions of the SP equation in the upper half complex time plane into equation (3), without the need to consider the choice of the integration contour, as we exemplified it in figure 2. A typical example is a linearly polarized monochromatic laser field for which there are two relevant SP solutions [23]. As further illustrations we utilized the examples of a bicircular laser field, a few-cycle laser pulse with sine-squared envelope and an orthogonally polarized two-color laser field. These fields have become very important in the context of recent developments of strong-field physics and attoscience and the use of tailored fields for the control of the microscopic attosecond-dynamics dynamics of quantum-mechanical processes driven by such fields. The contributions of different SP solutions to a given quantum-mechanical transition amplitude interfere in the fashion of Feynman's path integral [46] and quantum-orbit theory [4, 47–49]. Knowledge of these solutions and their behaviour as a function of the observable quantities (for example, the photoelectron momentum) enables better understanding and control of the strong-field processes. Physically, a larger imaginary part of a SP time solution implies a lower corresponding partial contribution to the ionization probability. (Recall that a vanishing imaginary part corresponds to $I_p = 0$).

In the present paper we have not considered modifications of the SFA theories due to the influence of the Coulomb potential (see the recent article [50] and references therein). Not going into detail, we mention that in these models one should solve the same or similar SP equation as those considered in our paper. Examples are the Coulomb-corrected SFA [51], the quantum trajectory-based Coulomb-corrected SFA [52], the Coulomb quantum-orbit SFA [53–55], the semiclassical two-step model [56] and the semiclassical approximation [57]. The results of our paper are relevant also in this context.

Explicit analytical results for the relevant matrix elements, given in the appendices, can also be used for the analysis of higher-order strong-field processes such as high-order harmonic generation and high-order above-threshold ionization. More about these processes can be found in the review articles [4–10]; for other approaches to the calculation of the high-order

harmonic generation amplitude see [58, 59] and references therein. The mentioned high-order processes can be considered as three-step processes. To each of these steps a particular saddle-point equation can be related. Strong-field ionization is the first step. The rule for the number of saddle-point solutions which we found in the present paper is useful for determining the saddle-point solutions for these high-order processes. For example, for the bicircular $r\omega$–$s\omega$ field we found $r+s$ solutions. For high-order above-threshold ionization [20] and high-order harmonic generation [36] we classified the SP solutions by the multi-index (α,β,m). The index $m=0,1,2,\ldots$ counts the approximate length of the electron travel time in multiples of the laser period T, the index α distinguishes the long from the short orbit, while the index β counts the segments (traced out by the bicircular field in the polarization plane) within one optical cycle characterized by the index m. There are exactly $\beta=1,2,\ldots,r+s$ solutions which agrees with the results of the present paper. Analogously, for the strong-field ionization by an $r\omega$–$s\omega$ OTC field there are $2s$ ($s>r$) solutions. Using the same classification by the multi-index (α,β,m) [45], we obtain that the index β takes $2s$ values. Knowing this makes it easier to find all SP solutions.

Acknowledgments

We acknowledge support by the Ministry for Education, Science and Youth, Canton Sarajevo, Bosnia and Herzegovina, the Federal Ministry of Education and Science, Bosnia and Herzegovina, and the Alexander von Humboldt Foundation.

Appendix A. *T*-matrix element for detachment of negative ions

For the detachment of the negative halogen ion F^-, which we considered as our first example, the ground-state wave function is [18, 19]

$$\psi_{\ell m}(\mathbf{r})=\frac{A}{r}\mathrm{e}^{-\kappa r}Y_{\ell m}(\hat{\mathbf{r}}), \tag{A.1}$$

with $A=0.7$, $l=1$ and $I_\mathrm{p}=3.4$ eV. The ground-state wave functions of other negative ions such as H^-, Cl^-, Br^-, I^- etc [19] have the same form, but with different values of the parameters A, ℓ and I_p. For the laser field defined in the xy plane and with the z axis as the atomic quantization axis only the matrix elements with $m=\pm1$ in (5) are different from zero. The corresponding momentum-space wave function $\tilde{\psi}_{\ell m}(\mathbf{q})=(2\pi)^{-3/2}A\int \mathrm{d}\Omega_{\hat{\mathbf{r}}}\int_0^\infty \mathrm{d}r r\mathrm{e}^{-\mathrm{i}\mathbf{q}\cdot\mathbf{r}-\kappa r}Y_{\ell m}(\hat{\mathbf{r}})$ can be calculated using the plane-wave expansion in spherical harmonics: $\mathrm{e}^{-\mathrm{i}\mathbf{q}\cdot\mathbf{r}}=4\pi\sum_{\ell=0}^\infty(-\mathrm{i})^\ell j_\ell(qr)\sum_{m=-\ell}^{\ell}Y^*_{\ell m}(\hat{\mathbf{r}})Y_{\ell m}(\hat{\mathbf{q}})$. Here $j_\ell(\rho)=\sqrt{\frac{\pi}{2\rho}}J_{\ell+\frac{1}{2}}(\rho)$ are the spherical Bessel functions. The result is

$$\tilde{\psi}_{\ell m}(\mathbf{q})=\frac{4\pi A}{(2\pi)^{3/2}}(-\mathrm{i})^\ell Y_{\ell m}(\hat{\mathbf{q}})X_\ell(q),\quad X_\ell(q)=\int_0^\infty \mathrm{d}r r\mathrm{e}^{-\kappa r}j_\ell(qr), \tag{A.2}$$

where the integral $X_\ell(q)$ can be solved analytically [60]. For $\ell=1$ we have $j_1(\rho)=-\rho^{-1}\cos\rho+\rho^{-2}\sin\rho$, so that

$$X_1(q)=-\frac{1}{q}\left(\frac{\kappa}{q^2+\kappa^2}-\frac{1}{q}\arctan\frac{q}{\kappa}\right). \tag{A.3}$$

Introducing this into (7) and using $Y_{1m}(\hat{\mathbf{q}}) = -m\sqrt{\frac{3}{8\pi}}\sin\theta_q \mathrm{e}^{\mathrm{i}m\phi_q}$ with $\mathrm{e}^{\mathrm{i}m\phi_q} = (q_x + \mathrm{i}mq_y)/q$, $\theta_q = 90°$, $q_x = q\cos\phi_q = p\cos\theta + A_x(t)$, $q_y = q\sin\phi_q = p\sin\theta + A_y(t)$, we obtain

$$T_{\mathbf{p}1m}(n) = m\mathrm{i}\frac{A\sqrt{3}}{4\pi}\int_0^T \frac{\mathrm{d}t}{T}\frac{q_x + \mathrm{i}mq_y}{q^2}\left(\kappa - \frac{q^2+\kappa^2}{q}\arctan\frac{q}{\kappa}\right)\mathrm{e}^{\mathrm{i}S(\mathbf{p};t)}. \quad \text{(A.4)}$$

According to (7) and (A.2), in order to apply the SP method, we should calculate the factor $\lim_{q^2+\kappa^2\to 0}(q^2+\kappa^2)X_\ell(q)$. It was shown in the appendix E of [19] that this factor is equal to $(q/\kappa)^\ell$. Using this, for the T-matrix element (A.4) in the SP approximation we get

$$T_{\mathbf{p}1m}(n) = C\sum_{t_s} B_m(t_s)\mathrm{e}^{\mathrm{i}S(\mathbf{p};t_s)}, \quad B_m(t_s) \equiv \frac{m(q_x + \mathrm{i}mq_y)}{\sqrt{\mathrm{i}S''(\mathbf{p};t_s)}}, \quad C = \frac{A}{\kappa T}\sqrt{\frac{3}{8\pi}}. \quad \text{(A.5)}$$

For the bicircular field, in addition to (20) and (21), in order to calculate the rate (4) using (7) and (A.4), we need the relations

$$\begin{aligned} E_x(t) &= \frac{1}{\sqrt{2}}\left[E_1\sin(r\omega t) + E_2\sin(s\omega t)\right], \quad E_y(t) = \frac{1}{\sqrt{2}}\left[-E_1\cos(r\omega t) + E_2\cos(s\omega t)\right], \\ \alpha_x(t) &= \frac{1}{\sqrt{2}}\left[\frac{A_1}{r\omega}\sin(r\omega t) + \frac{A_2}{s\omega}\sin(s\omega t)\right], \quad \alpha_y(t) = \frac{1}{\sqrt{2}}\left[-\frac{A_1}{r\omega}\cos(r\omega t) + \frac{A_2}{s\omega}\cos(s\omega t)\right], \quad \text{(A.6)} \\ U_1(t) &= \frac{A_1A_2\sin((r+s)\omega t)}{2(r+s)\omega}. \end{aligned}$$

For the elliptically polarized monochromatic laser field, used in section 3, we have $S(\mathbf{p};t) = n\omega t + pA_0\sin(\omega t)/(\omega\sqrt{1+\xi^2}) + U_\mathrm{p}\zeta\sin(2\omega t)/(2\omega)$. The T-matrix element in the uniform approximation is given by

$$\begin{aligned} T_{\mathbf{p}1m}(n) = C\sqrt{\pi}\mathrm{i}\Big\{&(\pm z)^{1/4}\left[B_m(t_2) \pm \mathrm{i}B_m(t_1)\right]\mathrm{Ai}(-z) \\ &+ \mathrm{i}(\pm z)^{-1/4}\left[-B_m(t_2) \pm \mathrm{i}B_m(t_1)\right]\mathrm{Ai}'(-z)\Big\}\mathrm{e}^{\mathrm{i}[S(\mathbf{p};t_1)+S(\mathbf{p};t_2)]/2}, \end{aligned} \quad \text{(A.7)}$$

where $z \equiv \left\{3\left[S(\mathbf{p};t_1) - S(\mathbf{p};t_2)\right]/4\right\}^{2/3}$. For the electron energy $E_\mathbf{p}$ larger than the critical value $E_{\mathbf{p},\mathrm{c}}$, for which the discriminant D in (10) is equal to zero, the argument of the Airy function Ai and its first derivative Ai$'$ should be replaced by $-z \to -z\mathrm{e}^{-2\pi\mathrm{i}/3}$. For $E_\mathbf{p} < E_{\mathbf{p},\mathrm{c}}$ ($E_\mathbf{p} > E_{\mathbf{p},\mathrm{c}}$) the sign + (−) should be taken in (A.7).

Appendix B. *T*-matrix element for ionization of noble gases

For ionization of noble gases, as the ground-state wave function of the valence electron we use the following asymptotic wave function [61]

$$\psi_{\ell m}(\mathbf{r}) = Ar^{\nu-1}\mathrm{e}^{-\kappa r}Y_{\ell m}(\hat{\mathbf{r}}), \quad r \gg 1. \quad \text{(B.1)}$$

For the Ne atom we have $\nu = 1/\kappa$ and $A = 2.1$, $\ell = 1$ and $I_\mathrm{p} = 21.56$ eV [20]. Expanding the plane wave in spherical harmonics and solving the appropriate integral [60], we obtain the momentum-space wave function

$$\tilde{\psi}_{\ell m}(\mathbf{q}) = \frac{A(-\mathrm{i}q)^\ell}{2^{\ell+\frac{1}{2}}\kappa^{\ell-\nu}}\frac{\Gamma(\ell+\nu+2)}{\Gamma(\ell+3/2)}\,{}_2F_1\left(\frac{\ell-\nu}{2}, \frac{\ell-\nu+1}{2}; \ell+\frac{3}{2}; -\frac{q^2}{\kappa^2}\right)\frac{Y_{\ell m}(\hat{\mathbf{q}})}{(q^2+\kappa^2)^{\nu+1}}, \quad \text{(B.2)}$$

where $\Gamma(\nu)$ is the gamma function and ${}_2F_1\,(a,b;c;z)$ the Gauss hypergeometric function, which is calculated numerically using the method from [62]. Introducing this into equation (7) we get

$$T_{\mathbf{p}\ell m}(n) = -\frac{A}{T}\frac{\kappa^\nu}{2^{\ell+3/2}}\frac{\Gamma(\ell+\nu+2)}{\Gamma(\ell+3/2)}\int_0^T \mathrm{d}t\left(\frac{q}{\mathrm{i}\kappa}\right)^\ell Y_{\ell m}(\hat{\mathbf{q}}) \\ \times\ {}_2F_1\left(\frac{\ell-\nu}{2},\frac{\ell-\nu+1}{2};\ell+\frac{3}{2};-\frac{q^2}{\kappa^2}\right)\frac{\mathrm{e}^{\mathrm{i}S(\mathbf{p};t)}}{\left(q^2+\kappa^2\right)^\nu}. \tag{B.3}$$

Since the T-matrix element (B.3) is singular at the SPs defined by (12), we cannot apply equation (6) directly. Instead, we use a modification of the SP method described in [18], which leads to the expansion

$$\int_C \frac{\mathrm{e}^{\mathrm{i}S(z)}}{[S'(z)]^\nu}\,\mathrm{d}z \approx \mathrm{i}^\nu\frac{\Gamma(\nu/2)}{2\Gamma(\nu)}\sum_j\sqrt{\frac{2\pi\mathrm{i}}{S''(z_j)}}\left[-\frac{2\mathrm{i}}{S''(z_j)}\right]^{\nu/2}\mathrm{e}^{\mathrm{i}S(z_j)}, \tag{B.4}$$

where z_j are the SPs of the analytic function $S(z)$. Applying formula (B.4) to solve the integral in equation (B.3), we obtain the following expression for the T-matrix element in the SP approximation

$$T_{\mathbf{p}\ell m}(n) = -\frac{A}{T}\frac{\kappa^\nu}{2^{\ell+\nu+3/2}}\frac{\Gamma(\ell+\nu+2)}{\Gamma(\ell+3/2)}\frac{\Gamma(\nu/2)}{2\Gamma(\nu)}\,{}_2F_1\left(\frac{\ell-\nu}{2},\frac{\ell-\nu+1}{2};\ell+\frac{3}{2};1\right) \\ \times\sum_{t_s}\left(\frac{q_s}{\mathrm{i}\kappa}\right)^\ell Y_{\ell m}(\hat{\mathbf{q}}_s)\sqrt{\frac{2\pi\mathrm{i}}{S''(\mathbf{p};t_s)}}\left[\frac{2\mathrm{i}}{S''(\mathbf{p};t_s)}\right]^{\nu/2}\mathrm{e}^{\mathrm{i}S(\mathbf{p};t_s)}. \tag{B.5}$$

For the special value $z=1$, the hypergeometric function ${}_2F_1$ can be written in terms of gamma functions:

$${}_2F_1(a,b;c;1) = \frac{\Gamma(c)\,\Gamma(c-a-b)}{\Gamma(c-a)\,\Gamma(c-b)},\quad \mathrm{Re}\,(c-a-b)>0. \tag{B.6}$$

Applying this expression and the properties of the gamma function we obtain our final form of the transition amplitude

$$T_{\mathbf{p}\ell m}(n) = -\frac{A}{T}\frac{\kappa^\nu}{2^{3/2}}\,\nu\Gamma(\nu/2)\sum_{t_s}\left(\frac{q_s}{\mathrm{i}\kappa}\right)^\ell Y_{\ell m}(\hat{\mathbf{q}}_s)\left[\frac{2\mathrm{i}}{S''(\mathbf{p};t_s)}\right]^{(\nu+1)/2}\mathrm{e}^{\mathrm{i}S(\mathbf{p};t_s)}. \tag{B.7}$$

Here $S(\mathbf{p};t) = (E_{\mathbf{p}}+U_\mathrm{p}+I_\mathrm{p})t+\mathbf{p}\cdot\boldsymbol{\alpha}(t)+U_1(t)$, where for our OTC field we have: $U_\mathrm{p} = (A_1^2+A_2^2)/4$, $\boldsymbol{\alpha}(t) = \alpha_1\sin(r\omega t)\hat{\mathbf{e}}_x+\alpha_2\sin(s\omega t+\phi)\hat{\mathbf{e}}_y$, $\alpha_1 = A_1/(r\omega)$, $\alpha_2 = A_2/(s\omega)$ and $U_1(t) = [\alpha_1 A_1\sin(2r\omega t)+\alpha_2 A_2\sin(2s\omega t+2\phi)]/8$.

ORCID iDs

D B Milošević https://orcid.org/0000-0001-5060-3318

References

[1] Keldysh L V 1964 *Zh. Eksp. Teor. Fiz.* **47** 1945

Keldysh L V 1965 *Sov. Phys.—JETP* **20** 1307
[2] Faisal F H M 1973 *J. Phys. B: At. Mol. Phys.* **6** L89
[3] Reiss H R 1980 *Phys. Rev.* A **22** 1786
[4] Becker W, Grasbon F, Kopold R, Milošević D B, Paulus G G and Walther H 2002 *Adv. At. Mol. Opt. Phys.* **48** 35
[5] Popov V S 2004 *Usp. Fiz. Nauk* **147** 921
Popov V S 2004 *Phys.—Usp.* **47** 855
[6] Ivanov M Y, Spanner M and Smirnova O 2005 *J. Mod. Opt.* **52** 165
[7] Milošević D B, Paulus G G, Bauer D and Becker W 2006 *J. Phys. B: At. Mol. Opt. Phys.* **39** R203
[8] Popruzhenko S V 2014 *J. Phys. B: At. Mol. Opt. Phys.* **47** 204001
[9] Nayak A *et al* 2019 *Phys. Rep.* **833** 1–52
[10] Amini K *et al* 2019 *Rep. Prog. Phys.* **82** 116001
[11] Gordon W 1926 *Z. Phys.* **40** 117
[12] Wolkow D M 1935 *Z. Phys.* **94** 250
[13] Bleistein N and Handelsman R A 1986 *Asymptotic Expansions of Integrals* (New York: Dover)
[14] Wong R 1989 *Asymptotic Approximations of Integrals* (Boston, MA: Academic)
[15] Leubner C 1981 *Phys. Rev.* A **23** 2877
[16] Lein M and Wollenhaupt M 2017 Special issue: Dynamics in tailored ultrashort light fields *J. Mod. Opt.* **64** 94
[17] Lewenstein M, Balcou Ph, Ivanov M Y, l'Huillier A and Corkum P B 1994 *Phys. Rev.* A **49** 2117
[18] Gribakin G F and Kuchiev M Y 1997 *Phys. Rev.* A **55** 3760
[19] Gazibegović-Busuladžić A, Milošević D B and Becker W 2004 *Phys. Rev.* A **70** 053403
[20] Milošević D B and Becker W 2016 *Phys. Rev.* A **93** 063418
[21] Paulus G G, Zacher F, Walther H, Lohr A, Becker W and Kleber M 1998 *Phys. Rev. Lett.* **80** 484
[22] Becker W, Kleber M, Lohr A, Paulus G G, Walther H and Zacher F 1998 *Laser Phys.* **8** 56
[23] Kopold R 2001 *Doctoral Dissertation* Technische Universität München
[24] Borovikov V A 1994 *Uniform Stationary Phase Method* (London: The Institution of Electrical Engineers)
[25] Fedoryuk M V 1987 *Asymptotics: Integrals and Series* (Moscow: Nauka) (in Russian)
[26] Figueira de Morisson Faria C, Schomerus H and Becker W 2002 *Phys. Rev.* A **66** 043413
[27] Milošević D B and Becker W 2002 *Phys. Rev.* A **66** 063417
[28] Čerkić A and Milošević D B 2006 *Phys. Rev.* A **73** 033413
[29] Milošević D B 2016 *J. Phys. B: At. Mol. Opt. Phys.* **49** 175601
[30] Eichmann H, Egbert A, Nolte S, Momma C, Wellegehausen B, Becker W, Long S and McIver J K 1995 *Phys. Rev.* A **51** R3414
[31] Long S, Becker W and McIver J K 1995 *Phys. Rev.* A **52** 2262
[32] Milošević D B, Becker W and Kopold R 2000 *Phys. Rev.* A **61** 063403
[33] Fleischer A, Kfir O, Diskin T, Sidorenko P and Cohen O 2014 *Nat. Photon.* **8** 543
[34] Chen C *et al* 2016 *Sci. Adv.* **2** e1501333
[35] Fan T *et al* 2015 *Proc. Natl Acad. Sci. USA* **112** 14206
[36] Milošević D B 2019 *J. Mod. Opt.* **66** 47
[37] Kramo A, Hasović E, Milošević D B and Becker W 2007 *Laser Phys. Lett.* **4** 279
[38] Hasović E, Kramo A and Milošević D B 2008 *Eur. Phys. J. Spec. Top.* **160** 205
[39] Odžak S, Hasović E, Becker W and Milošević D B 2017 *J. Mod. Opt.* **64** 971
[40] Milošević D B, Paulus G G and Becker W 2003 *Opt. Exp.* **11** 1418
[41] Milošević D B, Paulus G G and Becker W 2004 *Laser Phys. Lett.* **1** 93
[42] Shearer S F C and Monteith M R 2013 *Phys. Rev.* A **88** 033415
[43] Perry M D and Crane J K 1993 *Phys. Rev.* A **48** R4051
[44] Watanabe S, Kondo K, Nabekawa Y, Sagisaka A and Kobayashi Y 1994 *Phys. Rev. Lett.* **73** 2692
[45] Milošević D B and Becker W 2019 *Phys. Rev.* A **100** 031401
[46] Feynman R P and Hibbs A R 1965 *Quantum Mechanics and Path Integrals* (New York: McGraw-Hill)
[47] Kopold R, Milošević D B and Becker W 2000 *Phys. Rev. Lett.* **84** 3831
[48] Salières P *et al* 2001 *Science* **292** 902
[49] Milošević D B, Bauer D and Becker W 2006 *J. Mod. Opt.* **53** 125
[50] Milošević D B and Becker W 2019 *Phys. Rev.* A **99** 043411
[51] Popruzhenko S and Bauer D 2008 *J. Mod. Opt.* **55** 2573
[52] Yan T-M, Popruzhenko S V, Vrakking M J J and Bauer D 2010 *Phys. Rev. Lett.* **105** 253002

[53] Lai X-Y, Poli C, Schomerus H and Figueira de Morisson Faria C 2015 *Phys. Rev.* A **92** 043407
[54] Lai X-Y, Yu S-G, Huang Y-Y, Hua L-Q, Gong C, Quan W, Figueira de Morisson Faria C and Liu X 2017 *Phys. Rev.* A **96** 013414
[55] Maxwell A S, Al-Jawahiry A, Das T and Figueira de Morisson Faria C 2017 *Phys. Rev.* A **96** 023420
[56] Shvetsov-Shilovski N I, Lein M, Madsen L B, Räsänen E, Lemell C, Burgdörfer J, Arbó D G and Tőkési K 2016 *Phys. Rev.* A **94** 013415
[57] Milošević D B 2017 *Phys. Rev.* A **96** 023413
[58] Plaja L and Pérez-Hernández J A 2007 *Opt. Express* **15** 3629
[59] Frolov M V, Flegel A V, Manakov N L and Starace A F 2007 *Phys. Rev.* A **75** 063408
[60] Gradshtein I S and Ryzhik I M 1994 *Tables of Integrals, Series, and Products* (Boston, MA: Academic)
[61] Radzig A A and Smirnov B M 1985 *Reference Data on Atoms, Molecules and Ions* (Berlin: Springer)
[62] Pearson J W, Olver S and Porter M A 2017 *Numer. Algorithms* **74** 821